Research Article

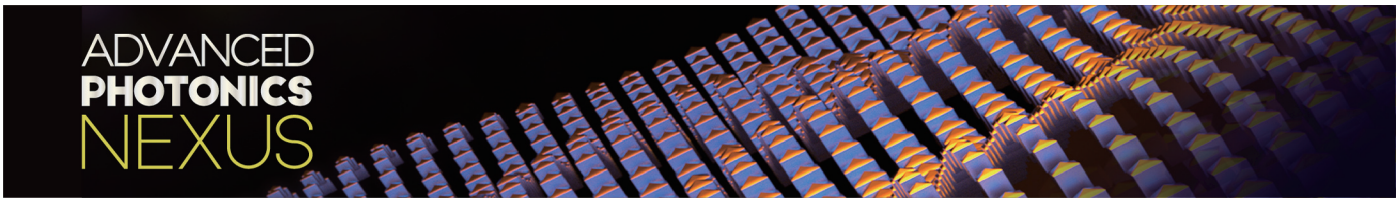

Multimodal fiber antenna for proximity and stress sensing

Merve Gokce,[a,†] Eilam Smolinsky,[a,†] Louis Alexandre van der Elst,[a,†] Jillian Noblet,[b] Creasy Clauser Huntsman,[b] and Alexander Gumennik[a,*]

[a]Indiana University, Luddy School of Informatics, Computing, and Engineering, Fibers and Additive Manufacturing Enabled Systems Laboratory, Department of Intelligent Systems Engineering, Bloomington, Indiana, United States
[b]Cook Medical Technologies, Bloomington, Indiana, United States

Abstract. Fiber sensors are commonly used to detect environmental, physiological, optical, chemical, and biological factors. Thermally drawn fibers offer numerous advantages over other commercial products, including enhanced sensitivity, accuracy, improved functionality, and ease of manufacturing. Multimaterial, multifunctional fibers encapsulate essential internal structures within a microscale fiber, unlike macroscale sensors requiring separate electronic components. The compact size of fiber sensors enables seamless integration into existing systems, providing the desired functionality. We present a multimodal fiber antenna monitoring, in real time, both the local deformation of the fiber and environmental changes caused by foreign objects in proximity to the fiber. Time domain reflectometry propagates an electromagnetic wave through the fiber, allowing precise determination of spatial changes along the fiber with exceptional resolution and sensitivity. Local changes in impedance reflect fiber deformation, whereas proximity is detected through alterations in the evanescent field surrounding the fiber. The fiber antenna operates as a waveguide to detect local deformation through the antisymmetric mode and environmental changes through the symmetric mode. This multifunctionality broadens its application areas from biomedical engineering to cyber–physical interfacing. In antisymmetric mode, the device can sense local changes in pressure, and, potentially, temperature, pH, and other physiological conditions. In symmetric mode, it can be used in touch screens, environmental detection for security, cyber–physical interfacing, and human–robot interactions.

Keywords: fiber antenna; waveguide; symmetric and antisymmetric modes; environmental proximity sensing; local physiological sensing; real-time monitoring.

Received Apr. 18, 2024; revised manuscript received May 26, 2024; accepted for publication Jul. 8, 2024; published online Aug. 16, 2024.

[DOI: 10.1117/1.APN.3.5.056011]

1 Introduction

Smart polymer-based monofilament fibers are an emerging technology that has found application in diverse fields. These fibers' distinctive properties stem from the ability to control the embedded multimaterial architecture of functional materials forming the embedded device, thus allowing for packaging an intricate functional modality in a thin, long, and flexible fiber form. Such fibers are excellent candidates for sensing various environmental, physiological, and biomechanical stimuli and can serve as an input interface for human–computer and human–robot interaction. The multifunctional characteristic of the monofilament fiber devices requires the embedded multimaterial architecture preserved through the device fabrication, as designed for optimized electronic performance. The thermal drawing technique provides uniformity of monofilament fiber devices over kilometers with complex geometries and material combinations embedded into the fiber cladding.[1–5] It allows, starting from the preform, which is a cross-sectionally scaled-up and longitudinally scaled-down replica of the desired fiber device, typically centimeters wide and meters long, to translate the cross-sectional geometry from the preform to the fiber, typically hair-thin and kilometers long, nominally unperturbed,

*Address all correspondence to Alexander Gumennik, gumennik@iu.edu
†These authors contributed equally to this work.

just uniformly scaled down to the desired device dimensions. Multimaterial thermally drawn fibers with polymer claddings are designed to be responsive to a variety of signals, such as stress,[6] temperature,[7] human motion,[8] magnetic actuation,[9] and the presence of chemicals.[10] Smart polymer fibers can be integrated into constructs with added functionality, such as smart textiles,[11] more complex wearable electronics,[12,13] and implantable sensors and transducers.[14]

The ability to control the cross-sectional architecture of the multimaterial fiber at the microscale[15,16] allows packaging electromagnetically guiding conductive domains along the fiber's length, organized in a defined geometry that facilitates waveguiding in a gigahertz to terahertz range. Radiation propagates along the power line packaged into the fiber's cross section. In contrast, the externally induced changes to the local impedance of the power line, either through the deformation of the fiber itself or the insertion of the foreign object into the evanescent field of the propagating mode, create scattering, which the operator can sense as the change to the forward-propagating, as well as backreflected signal.

This paper presents an electromagnetically multimodal fiber antenna that offers real-time monitoring capabilities for environmental and, potentially, physiological parameters, providing functionally multimodal sensing capabilities. The sensing capability of the fiber antenna in a multiplicity of functional modalities broadens its potential application areas as follows: (1) monitoring environmental signals, such as pressure, temperature, and proximity; (2) physiological signals, such as blood pressure and body temperature; (3) human–robot interactions as gesture control; and (4) cyber–physical systems, such as networking, information, and communication (as illustrated in Fig. 1). This study reports the multimodal fiber antenna's pressure- and proximity-sensing capabilities in symmetric and antisymmetric modes. Furthermore, regarding environmental signal monitoring, making specific modifications to the architecture of the fiber device presented in this study could facilitate the detection of humidity and pH levels. For both environmental indicators, exposing the core wires is necessary. Our previous work demonstrated this process,[18] where metal cores were periodically exposed along the fiber by selectively breaking and etching a sacrificial core into periodic outlets.[16] For a humidity sensor, the cores would be isolated from each other, allowing the detection of environmental humidity based on resistance measured between the two core wires. For a pH sensor, one of the two cores would be converted to a reference pH material. This setup would analyze the difference between the unexposed reference core and the exposed wire, mimicking the process commonly used in pH meters.

2 Thermal Drawing of Multimodal Fiber Antenna Sensor

The thermal drawing process of the smart fibers begins with the preparation of a macroscale preform. The macroscale preform is drawn to a microscale fiber under defined drawing conditions, including a set draw temperature, preform feed speed, and fiber draw speed. The preform, composed of cladding and core materials in a specific geometry, is fabricated using various techniques such as 3D printing,[15,19,20] thin-film rolling, and other conventional methods, such as stacking and consolidation of macroscale multimaterial domains.[21] Thermal drawing parameters are carefully controlled to preserve the cross-sectional geometry of the preform during the fiber drawing process. The resulting thickness of the fiber, with respect to the thickness of the preform, is controlled by the ratio between the preform feed speed and fiber draw speed, as described by the equation provided in Fig. 2(a). Meticulous control of the defined parameters ensures consistency and accuracy in producing multimaterial fibers with specific cross-sectional geometries and dimensions, enabling different functional capabilities.

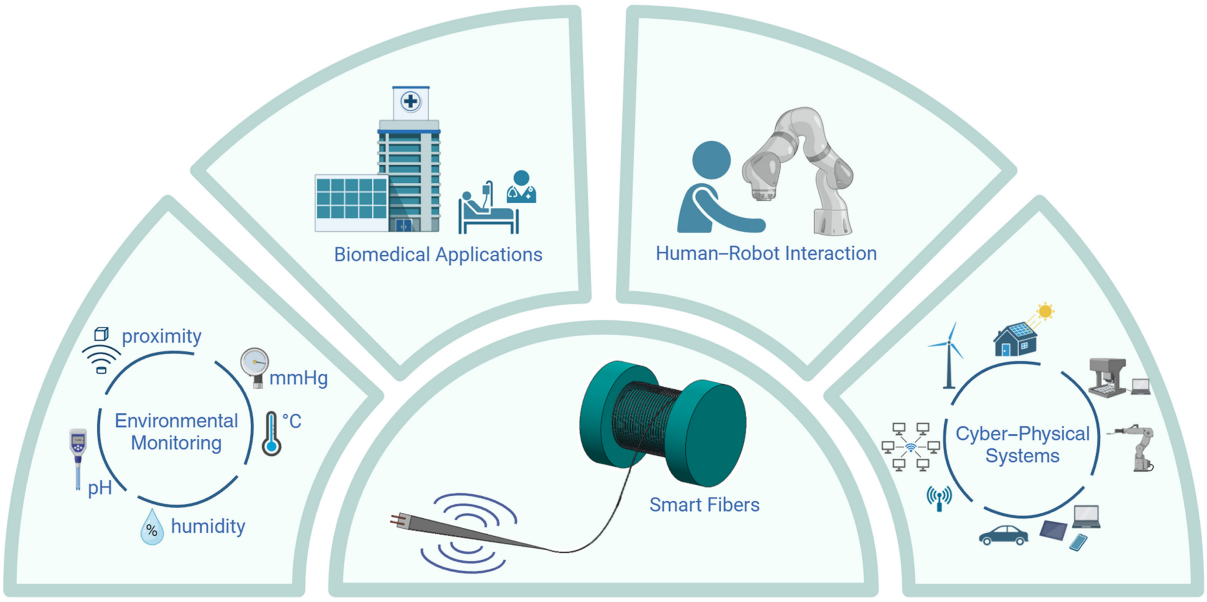

Fig. 1 Application areas of multimodal fiber antenna sensor including environmental monitoring, biomedical applications, human–robot interactions, and cyber–physical systems. Figure created with permission from Ref. 17.

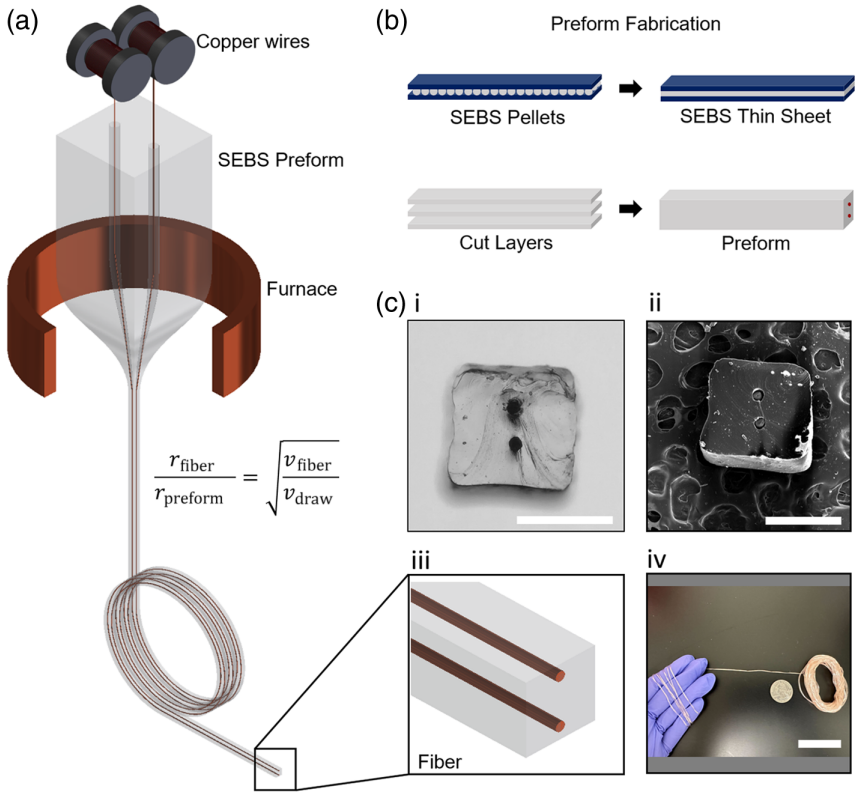

Fig. 2 (a) Thermal drawing of the multimodal fiber antenna sensor. (b) The preform fabrication steps. (c)-i. Cross-sectional image of the fiber sensor under an optical microscope (4× magnification, scale bar = 500 μm). (c)-ii. SEM image of the fiber sensor (FEI Quanta 600, scale bar = 500 μm). (c)-iii. Close-up illustration capturing the drawn fiber, showcasing its maintained cross-sectional geometry and enclosed parallel copper wires. (c)-iv. Photo displaying 600-μm diameter, and 65 m of drawn fiber coiled around a hand. 2.42 cm quarter coin shows the scale of the coiled fiber (scale bar = 5 cm).

The preform of the multimodal fiber antenna contains a thermoplastic elastomer as the cladding material, styrene–ethylene–butylene–styrene (SEBS, Kraton G1657, Houston, Texas, United States), and two parallel copper wires as the core materials, with a diameter of 75 μm (Goodfellow, 99.9% copper, annealed, Pittsburgh, Pennsylvania). The copper wires were introduced into the preform using a custom-designed 3D-printed feeding cap during the fiber drawing process. This cap was positioned atop the preform holder where the two wire spools unwound, guiding the alignment of the two copper wires in parallel. Both wires were confined into the SEBS cladding simultaneously while the fiber was pulled by a capstan.[18] The preform was heated within a furnace maintained above the polymer's glass transition temperature to soften the polymer cladding. The hot zone of the furnace was maintained at ~200°C according to our pyrometer reading. The fiber is drawn by the capstan and spooled on a reel below the furnace at the set draw speed (3 m/min increased incrementally to 15 m/min), as schematically depicted in Fig. 2(a). Fabricating the fiber antenna's preform involves consolidating multiple SEBS layers made from heated and pressed SEBS pellets. These SEBS pellets were heated at 200°C for 2 to 3 h to create SEBS films with a thickness of 2 mm. Subsequently, the SEBS films were cut into multiple 3 cm wide ribbons. A 2 mm wide centered channel was cut out of two SEBS ribbons to create parallel channels to feed copper wires through the preform later during the draw. Vertically stacked SEBS ribbons form a 3 cm by 3 cm square preform, consolidated in a vacuum oven at 175°C for 2 h [as depicted in Fig. 2(b)]. Imaging the fiber cross sections under the light and scanning electron microscopes confirms the resulting square cross-sectional geometry with parallel copper wires confined inside the SEBS cladding [Fig. 2(c)-i–iii]. Tens of meters of fiber antenna were drawn in 42 min [see Fig. 2(c)-iv].

3 Stress and Proximity Sensing by Time-Domain Reflectometry

3.1 Working Principle of Multimodal Fiber Antenna Sensor for Pressure and Proximity Sensing

Electronic characterization of the multimodal fiber antenna was performed by time-domain reflectometry (TDR). TDR sends a step function electromagnetic pulse with a rise time of a few picoseconds onto the power line formed by the fiber-embedded copper wires and "listens to the echo" coming from the scattering centers along the fiber created by either a change in pressure or proximity signals with a bandwidth of 35 GHz. The amplitude of the reflected echo increases with the strength of the signal measured. The time delay between incoming and reflected signals resolves the locations along the fiber where the signal is created. In other words, TDR transforms time domain stimulus into space domain signal, according to Eq. (1),

$$T = \frac{2 \cdot n_{\text{eff}} X}{c}, \tag{1}$$

where T is the time after the voltage step, X is the location, n_{eff} is the effective refractive index of the mode, and c is the speed of light. We measured the signal from several known locations on the fiber, which, using Eq. (1), gave $n_{\text{eff}} = 1.41 \pm 0.02$ for the antisymmetric mode (mode 1).

In this case of a multimodal fiber antenna sensor, two parallel copper wires function as transmission lines to the electromagnetic wave sent by the TDR in the elastic SEBS dielectric medium. The impedance Z of the two-wire transmission line is calculated using Eq. (2),[21] assuming an insulating medium and highly conductive wires,

$$\begin{cases} Z = \sqrt{L/C} = \frac{1}{\pi}\sqrt{\mu/\varepsilon} \cdot \cosh^{-1}(d/a) \propto 1/C \\ C = \frac{\pi \varepsilon_{\text{eff}}{}^{1}}{\cosh^{-1}(d/a)} \\ L = \mu/\pi \cosh^{-1}(d/a), \end{cases} \tag{2}$$

where $\varepsilon = \varepsilon_r \varepsilon_0$ is the permittivity of the volume and μ is its permeability, d is the distance between two wires, a is the diameter of the wires, and ε_r is the dielectric constant. $\varepsilon_{\text{eff}}{}^{1}$ is the permittivity of the fiber in mode 1, and L and C, the lengthwise inductance and capacitance between the wires, are the analytical solutions for an infinite fiber length approximation, respectively. The mode-specific ε, i.e. $\varepsilon_{\text{eff}}{}^{i}$, where i is the mode number, is determined by the fact that ε_r of a given mode relates to the n_{eff} of that mode through $\varepsilon_r = n_{\text{eff}}{}^{2}$. Still, the theoretical Z agreed well with the simulations and measurements.

The TDR generates the voltage step in the fiber in two principal modes. The symmetrical mode (mode 0), also known as a Sommerfeld–Zenneck[22,23] wave, interacts strongly with the environment but is almost insensitive to fiber deformations, since most of the electric field is away from the two wires, forming large-area mode with significant evanescent field surrounding the fiber with almost no field between the electrodes. The diffraction limit of electromagnetic radiation at the frequency range in which TDR is operated is significantly larger than the fiber diameter, hence the significant distance of the symmetric mode evanescent field penetration into the fiber surrounding. The antisymmetric first mode is strongly localized between the wires, with only a weak evanescent wave outside the fiber. This mode is almost completely insensitive to changes in the environment of the fiber but strongly scatters from deformations in the fiber. The difference between the modes is clearly manifested in Fig. 4.

The propagating zero mode will scatter from changes in the effective refractive index of the fiber, resulting from changes in the dielectric environment outside the fiber, according to

$$\frac{\Delta V}{V_0} = \frac{\Delta n_{\text{eff}}}{2n_{\text{eff}} + \Delta n_{\text{eff}}} \approx \frac{\Delta n_{\text{eff}}}{2n_{\text{eff}}} \approx \frac{\Delta \varepsilon_{\text{eff}}{}^{0}}{4\varepsilon_{\text{eff}}{}^{0}}, \tag{3}$$

where V_0 is the height of the voltage step, ΔV is the measured change in reflected/transmitted voltage. $\varepsilon_{\text{eff}}{}^{0}$ and $\Delta\varepsilon_{\text{eff}}{}^{0}$ are the permittivity and the change in the permittivity, respectively, in mode 0 due to the changes in the fiber environment. Δn_{eff} is the change in each mode's refractive index due to the changes in the fiber environment.

The first mode derives its refractive index almost exclusively from the refractive index n of the medium of the fiber with $n = \sqrt{LC}/c = \sqrt{\varepsilon_r}$ but is reflected from locations, where mode's cross-sectional field distribution gets distorted, which can be expressed analytically as[24]

$$\frac{\Delta V}{V_0} = \frac{\Delta Z}{2Z + \Delta Z} \approx \frac{\Delta Z}{2Z} \propto \frac{\Delta C}{C}. \tag{4}$$

ΔZ and ΔC are the changes in the impedance and capacitance, respectively, at the fiber's mode-distortion site. Such distortion can be created, for instance, by a local fiber deformation due to pinch. The electromagnetic coupling scheme of the fiber antenna is shown in Fig. 3(a), where one of the copper wires is connected to the TDR module, and the other one is grounded. The TDR was used to measure the local change in the signal voltage at the scattering centers. A reference baseline signal for the pressure measurements was collected when no weight is added to the pedestal sitting on the fiber, while for the proximity measurement – with no foreign objects (including the pedestal) in the fiber surrounding. Metal weights of different sizes were systematically positioned along the fiber to assess the pressure-sensing capability of the multimodal fiber antenna. These weights were placed onto 3D-printed 1 cm wide plastic pedestals, precisely directing the applied load onto specific, measurable local areas of the fiber antenna while keeping the added weights away from the evanescent field of the fiber modes, such that the stress due to the added weight is sensed exclusively, without the interference with the proximity signal. The change in the distance between two parallel wires alters the capacitance, and thus the overall impedance, leading to local voltage changes, according to Eqs. (2) and (4) [refer to Fig. 3(b)].

The multimodal fiber antenna effectively detects foreign objects, such as metal weights within the fiber proximity (d_{mode}), using the same setup but without the intermediary pedestal between the fiber antenna and the weights. Detected in this scheme is the change in the reflected signal voltage due to the changes in the fiber's dielectric environment, as described in Eq. (3) [see Fig. 3(c)].

3.2 Multiphysics Simulations of Electromagnetic Coupling

The electromagnetic coupling scheme shown in Fig. 3(a), where one wire connects to the TDR while the other is grounded, generates a weighted sum superposition of symmetric and antisymmetric modes. To analyze their sensitivity to pressure and proximity, the modes of the multimodal fiber antenna sensor were simulated separately using the COMSOL Multiphysics electromagnetic module.[25] Material properties, including relative permittivity and permeability of SEBS, copper, and air, were integrated into the physics of the electromagnetic module, along with the cross-sectional geometry of the fiber sensor.

As expected, the symmetrical mode of the fiber propagates as a radially polarized field with a significant portion outside the fiber cladding (decaying as $\sim 1/r$), with almost no field at the center [Fig. 4(a)-i], whereas the antisymmetric mode is formed by a much better-confined electric field at the center [Fig. 4(a)-ii], with a negligible dipole field outside the fiber cladding. The effects of both deformation and changes in the environment were studied for both modes by simulating a 2% deformation on the fiber due to applied stress and introducing

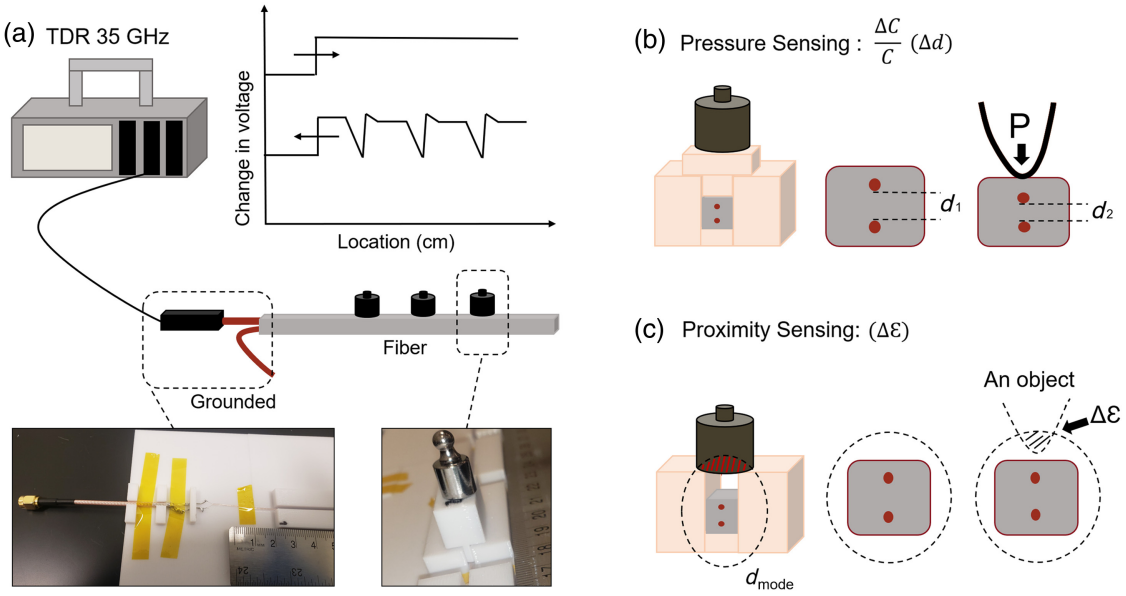

Fig. 3 (a) Electromagnetic coupling scheme of multimodal fiber antenna sensor and TDR. (b) Principle of pressure sensing of fiber sensor by change in the capacitance due to change in the distance between metal wires. (c). Principle of proximity sensing of fiber sensor by change in the dielectric environment of the fiber.

a foreign object located 0.7 mm away from the center of the fiber. Calculated changes in the fiber's refractive index and impedance reveal which fiber mode is best suited for pressure or proximity monitoring.

Placing a foreign object (1 mm diameter sphere with a dielectric constant of 2) 0.4 mm away from the fiber sensor noticeably distorts the symmetric mode 0 [Fig. 4(b)-i], whereas the antisymmetric mode [Fig. 4(b)-ii] shows no discernible change. These changes in the fiber sensor's refractive index and impedance are summarized in Table 1. Mode 0, as the symmetric mode, exhibits a significantly higher change in the refractive index of 1.045% for proximity measurement compared with a 2% deformation, whereas antisymmetric mode (mode 1) displays changes of 1.551%, with almost no impact on proximity measurements.

The mode analysis model provided us with the effective refractive index of each mode, whereas the impedance was calculated as $Z = V/I$, where V was obtained by integrating the electric field along the line between the wires (red line), and I was obtained by integrating the magnetic field along the circle that contained one of the wires (green contour). The change in the impedance due to the emergence of the scattering center provides a practical measure of the respective mode geometry deformation.

From Table 1, it is apparent that for the symmetric mode, the scattering resulting in the detection of backreflection is a result of a local change in refractive index at the location of foreign object introduction into the fiber proximity, whereas, for the antisymmetric mode, it is a result of a mismatch in the mode geometry between the deformed fiber location and the rest of the fiber.

4 Electronic Characterization of Multimodal Fiber Antenna Sensor by TDR

The sensitivity and spatial resolution of the multimodal fiber sensor were characterized using TDR for pressure and proximity responses. The multimodal nature of the fiber allowed for clear differentiation between pressure and proximity sensing, with a high signal-to-noise ratio.

The sensitivity curve of the fiber sensor was analyzed by applying pressure along the fiber using metal weights varying from 1 to 100 gr distributed along the fiber with 10 cm separation for the vertical and horizontal wire measurement configurations. The weights were placed on a 1 cm long pedestal on top of the 600 μm wide fiber. The TDR resolved the change in the backreflected signal at each location where the pressure was applied. The sensitivity of the fiber sensor was analyzed for the copper wires' horizontal and vertical configuration. Applying pressure in the measurement configuration where the wires are aligned horizontally (stress direction is perpendicular to the wire-dipole axis) increased the distance d between wires, resulting in a positive ΔZ [refer to Fig. 5(a)]. Conversely, applying pressure vertically (stress direction along the wire-dipole axis) decreased d, causing a negative ΔZ [refer to Fig. 5(b)]. As expected, the two configurations generated opposite signals, with the vertical signal approximately twice as strong as the horizontal one, due to Poisson's ratio relating the two types of resulting linear strains at the same stress.

Sensitivity limits were analyzed using lower weights such as 1, 2, and 5 gr at the 9.5 cm distance from the fiber–TDR module connection. The highest noise-equivalent pressure of 0.274 kPa was recorded for a weight of 1 gr, distributing the load over 1 cm of fiber ~0.6 mm wide, effectively applying stress of ~1.7 kPa. Thus, for any pressure smaller than 1.7 kPa, the noise equivalent signal is equal to or smaller than 0.274 kPa [see Fig. 5(c)]. Spatial resolution was determined as the full width at half-maximum (FWHM) of the locally observed change in voltage along the fiber [see Fig. 5(d)], measured for the 1 cm pedestal. A multipoint pressure analysis was conducted along the entire 50 cm fiber length, with 50 gr weights placed at 9.5, 17, 27.5, 37.5, and 47 cm. Consistent and significant changes in voltage were observed at each location along the fiber [see Fig. 5(e)].

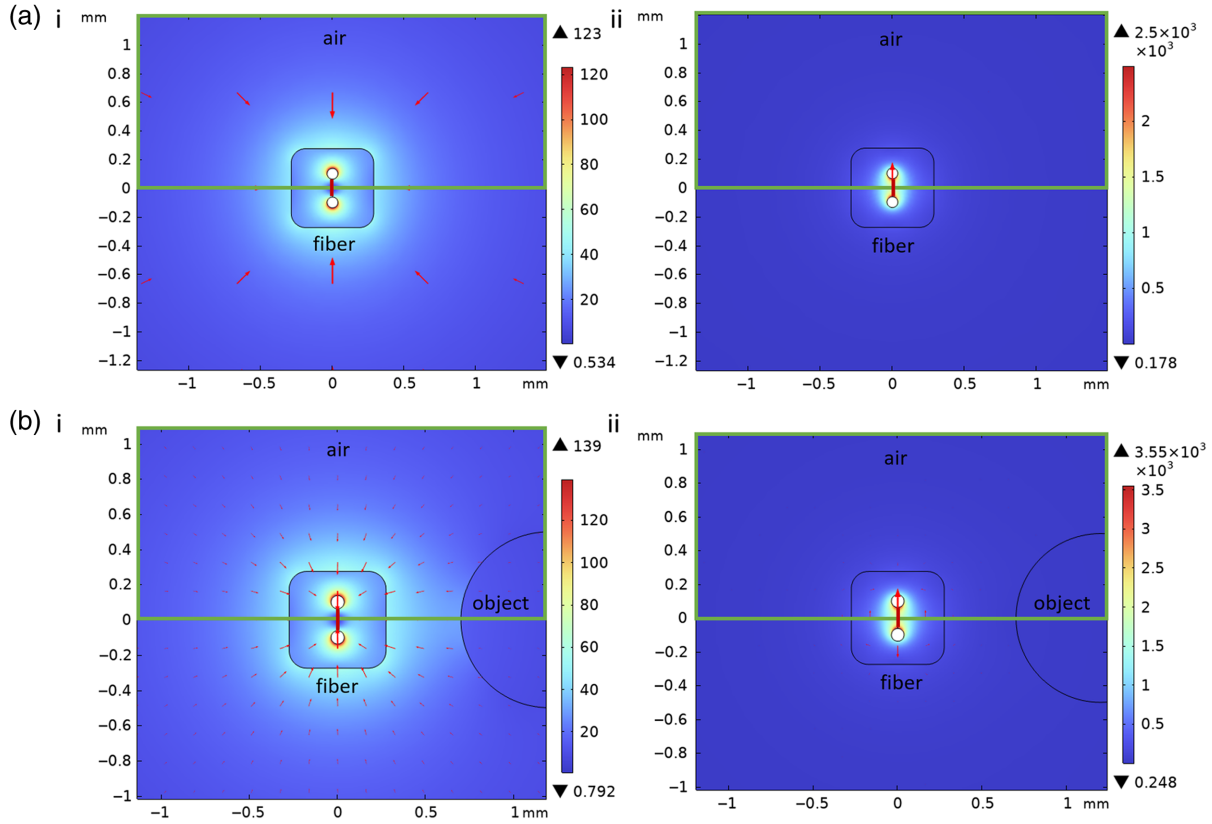

Fig. 4 Electromagnetic field FEM simulation using COMSOL Multiphysics. (a)-i. Field surrounding the fiber sensor at fiber mode 0 (symmetric). (a)-ii. Field surrounding the fiber sensor at fiber mode 1 (antisymmetric). (b)-i. Field surrounding the fiber sensor at fiber mode 0 with the presence of a foreign object within the fiber's diffraction limit. (b)-ii. Field surrounding the fiber sensor at fiber mode 1 with a foreign object within the fiber's diffraction limit. The simulations are conducted at a frequency of 18 GHz, a characteristic median frequency for pulses generated by electronics operating in a frequency band of up to 35 GHz. The fiber device cladding has a filleted-corner square cross section with a side of 600 μm. The dielectric constant is 2 for both the SEBS fiber cladding and the foreign object brought into the fiber proximity.

Table 1 Changes in the fiber sensor's refractive index and impedance at mode 0 (symmetric mode) and mode 1 (antisymmetric mode) for deformation and proximity studies. Notations: O (10^{-x}) is "order of 10^{-x}."

	Change in refractive index (Δn)		Change in impedance (ΔZ)	
	Mode 0 (%)	Mode 1 (%)	Mode 0	Mode 1
2% deformation	0.177	0.078	O (10^{-6} Ω)	2.23 Ω (1.551%)
Foreign object at 0.4 mm away	1.045	0.021	O (10^{-6} Ω)	0.39 Ω (0.27%)

The proximity response of the fiber sensor was assessed using 2 gr (7 mm wide), 50 gr (18 mm wide), and a finger placed at the 8 cm location along the fiber sensor without placing the pedestal on top of the fiber. Since the depth of the groove in the fiber holder [Fig. 3(a)] is 5 mm, and the fiber itself is 0.6 mm thick, which defined a distance of 4.7 mm from the proximity-effect scattering-inducing object and the fiber center. Proximity measurements indicate a difference in the signal shape for different materials, as the shape and size of the peaks change between the weights and wider peaks of the finger [see Fig. 5(f)].

The refractive indices for antisymmetric and symmetric modes varying as a function of frequency in the computationally attainable frequency range (0.8 to 35 GHz) indicate the dispersion of the electromagnetic wave propagating through the fiber antenna [Fig. 6(a)]. Simulations below 0.8 GHz frequency were not reliable due to the emergence of random calculation errors, indicated by the growing dependence of the finite-element method (FEM) calculations on the mesh granularity. In addition, the radius curvature of the metal wires becomes orders of magnitude smaller compared to the wavelength at lower frequencies, making the directionality of the polarization and electric field at the boundary between the wire and the cladding indefinable, resulting in exploding error in FEM calculation for frequencies lower than 0.8 GHz.

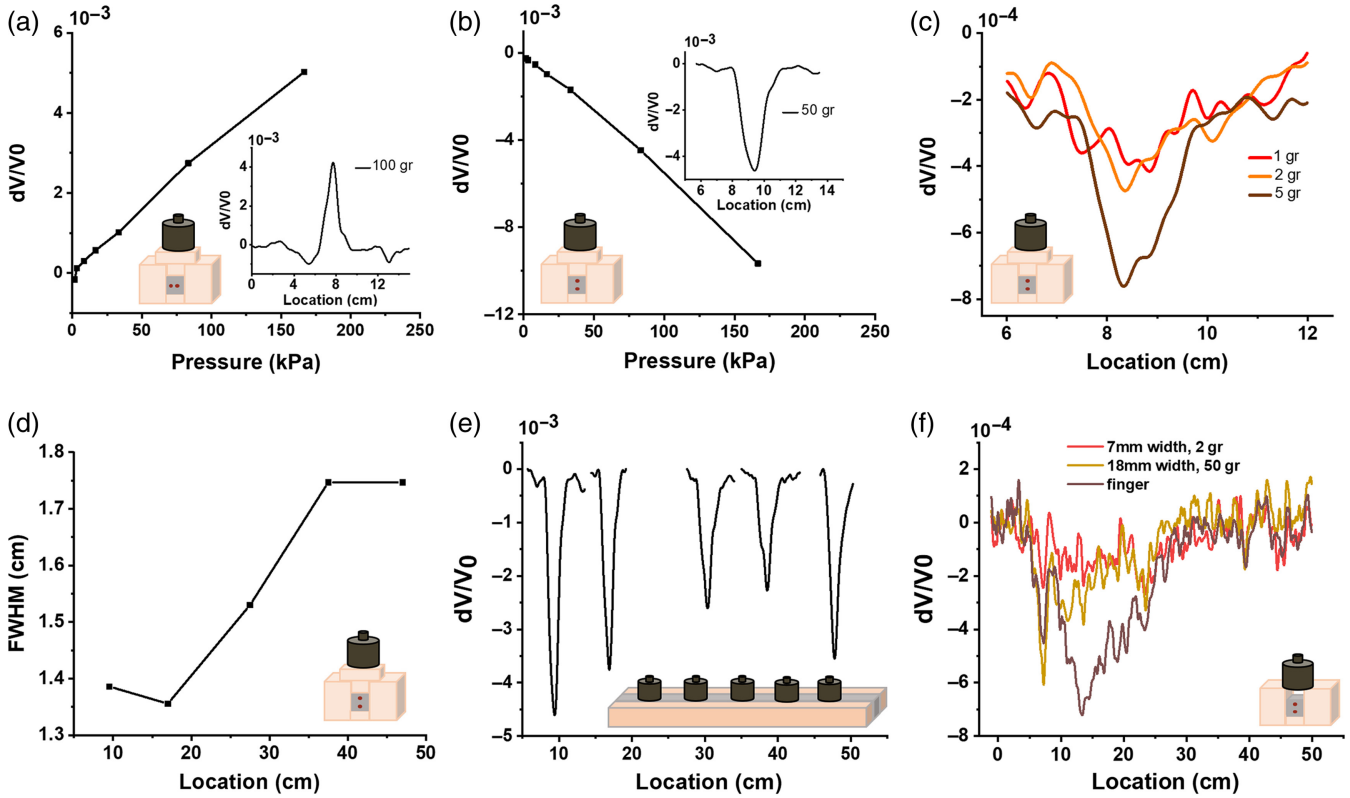

Fig. 5 TDR measurements of the multimodal fiber antenna under different configurations. (a) The sensitivity curve when the metal wires are placed horizontally (horizontal configuration). Inset, an example of a measurement with 100 gr. (b) The sensitivity curve when the metal wires are placed vertically (vertical configuration). Inset, an example of a measurement with 50 gr. (c) Sensitivity measurements in the vertical configuration, using light weights of 1, 2, and 5 gr. (d) Spatial resolution in the vertical configuration. (e) Distributed pressure measurement using 50 gr at 9.5, 17, 27.5, 37.5, and 47 cm in the vertical configuration. (f) Proximity measurement without the plastic pedestal used in the pressure measurements. The weights used in this case have a footprint diameter of 7 and 18 mm for the 2 and 50 gr weights, respectively. In addition, an index finger with a width of ~13 mm is used in the measurements.

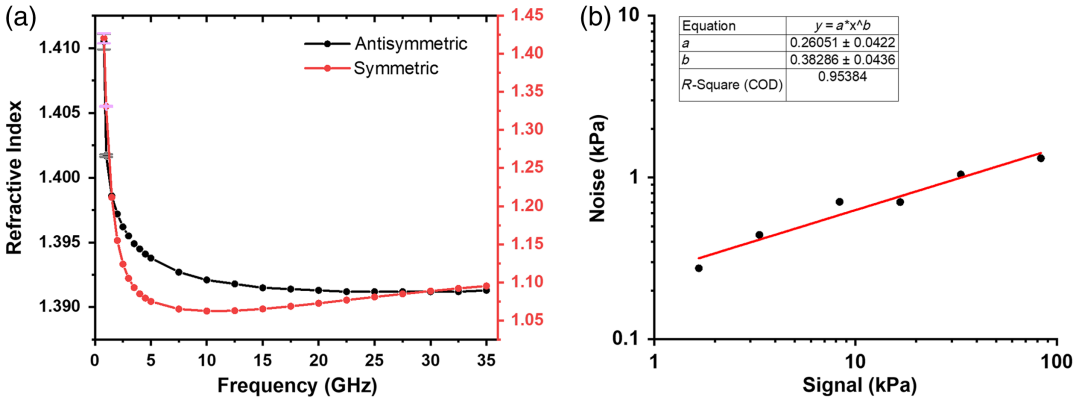

Fig. 6 Signal analysis of fiber antenna evaluating dispersion and sensitivity. (a) The refractive indices of the fiber at antisymmetric and symmetric modes are simulated at the frequency range of 0.8 to 35 GHz by COMSOL Multiphysics simulations. 0.8 and 1 GHz results of mode refractive index have error bars indicating increasing sensitivity to the mesh fineness. (b) Signal-to-noise graphic of the fiber antenna with vertical wire configuration using 1 to 50 gr weights indicates an increase in noise relevant to an increase in signal. The power function fitting shows the sensitivity limit of the fiber antenna as 0.26 kPa.

From a practical standpoint, the lower limit of frequency participating in the signal measurements is actually higher than 0.8 GHz. Looking at Fig. 5(d), we see that the FWHM of the signal peak in pressure measurements does not exceed 1.8 cm. Thus, wavelengths λ of radiation for which 1.8 cm is smaller than the diffraction limit $\lambda/2$ do not participate significantly in forming that signal. For the symmetric mode, this would correspond to all the frequencies below 8.3 GHz, and for the antisymmetric mode—to the frequencies below 6.0 GHz.

The calculated mode dispersion curves show that the dispersion of the modes in the relevant frequency ranges, i.e., 8 to 35 GHz for the symmetric mode and 6 to 35 GHz for the antisymmetric mode, is much more pronounced for the symmetric mode than for the antisymmetric mode. Since the diameter of the symmetric mode is comparable to the diffraction limit of the wavelength and counterproportional to the frequency, its field penetrates deeper into the air as the wavelength increases, further deviating from the refractive index of the fiber material. The antisymmetric mode, on the other hand, is mainly confined between the two wires within the body of the fiber. In this confinement configuration, the mode index is primarily defined by the cladding material and is not affected much by the frequency change at any reasonable frequency. In turn, the refractive index of the antisymmetric mode is only weakly sensitive to frequency.

Signal dispersion can be evaluated by $\Delta n/n$, where Δn is the refractive index difference between the fastest- and slowest-propagating frequencies on the dispersion curve, and n is the average refractive index for the given mode in the relevant range of frequencies. $\Delta n/n$ is equivalent to $\Delta L/L$, where ΔL is a spatial pulse broadening of the signal after propagating distance L.

The computed dispersion shown in Fig. 6(a) indicates $\Delta n/n = 0.027$ for symmetric mode in the range of frequencies 8 to 35 GHz and 0.0018 for antisymmetric mode in the range of frequencies 6 to 35 GHz.

Figure 5(d) indicates the experimental $L = 37.5$ cm as the propagated distance difference between the closest and farthest propagating signals, measured at 9.5 and 47 cm, respectively, and $\Delta L = 0.4$ cm as the change in the FWHM of the signals in this propagated distance difference. Thus, experimental $\Delta L/L = 0.01$. The experimental $\Delta L/L$ falls between the calculated values of $\Delta n/n$ for the two modes. This is an expected outcome since the real-world signal is a superposition of the two modes.

Figure 6(b) shows the measured noise equivalent pressure as a function of the signal for the fiber with vertical wire configuration. The noise equivalent signal is calculated as the standard deviation in the baseline, i.e., the signal fluctuations read at the locations where no pressure is applied. Without losing generality, we can claim that the two noise sources are Shot and Johnson noise.

For a fixed bandwidth, as in our case, Johnson noise, which is thermal noise, is independent of the signal amplitude, and Shot noise monotonically increases with the signal, as is expected from such a Poisson-statistics noise. Power fit $y = a \cdot x^b$ indicates that for reasonable pressures, $a = 0.26 \pm 0.04$ kPa, and $b = 0.38 \pm 0.04$. This analysis yields the ultimate sensitivity limit of 0.26 ± 0.04 kPa defined by Johnson noise. In addition, the noise grows with signal monotonically in a manner closely resembling Shot noise behavior, even though pure Poisson noise b is expected to be 0.5.

5 Discussion and Future Directions

From the investigation in Fig. 4 and the conclusions stemming from it summarized in Table 1, the electromagnetic mode selectiveness greatly affects the selectiveness of the sensing modality. On the one hand, the symmetric mode, equivalent to the recently extensively investigated Zenneck wave,[23,26] has a significant component of the electric field penetrating substantially outside the cladding into the fiber surrounding; thus, it is susceptible to the local change in electromagnetic mode refractive index, resulting from foreign objects hovering in the fiber proximity. Such index changes create scattering, resulting in sensing events. The cross-sectional area of the symmetric mode is defined by the diffraction limit of the mode, increasing for the decreased electromagnetic frequency. It is thus expected that lowering the frequency while operating in symmetric mode will increase the distance away from the fiber at which the objects could be detected. This is important for applications such as surveillance and environmental sensing. Material selectivity in remote sensing can be improved through machine-learning algorithms trained to recognize specific signal shapes (i.e., the characteristic functional dependence of normalized voltage on distance) due to the fact that, as shown in Fig. 5(f), the shape of the signal depends on the foreign object material for the same characteristic size of the object—it is "sharper" (more concentrated around the object location) for metal than for living tissue, for instance. The last is critical for cyber–physical interfacing and secure human–robot interaction, since sensing and distinguishing a human (living tissue) from a tool (metal) prior to impact is crucial for operator safety in environments where humans perform cooperative tasks with robots.

On the other hand, the antisymmetric mode has most of its field concentrated between the electric leads of the power line. It is almost exclusively sensitive to fiber cross-sectional deformation and, thus, the better candidate for selective stress sensing. We argue that improving the deformability of the cladding by introducing porosity with an optimized pore density and size, specifically through 3D printing of the fiber preform, in similar ways to those applied to other biomedical devices,[27] reaching the superior sensitivity of sub 0.1 kPa, is critical for the competitive applicability of this technology in medical applications. In addition, selectivity in sensing specific types of stress, i.e., pinch, torsion, bending, stretching, compression, or hydrostatic pressure using machine-learning and artificial-intelligence algorithms[28] can potentially be applied if a statistically significant training set of signal shape versus the type of stress for such algorithms is generated. The ability to reliably distinguish the stress types is critical for the usefulness of the fiber in specific products aimed at specific applications, such as shape sensing,[29] gesture reading,[30] fracture detection and failure control in constructional and automotive composites,[31] and physiological monitoring.

Finally, molten-phase postprocessing techniques[32–36] can be employed to upgrade the fiber antenna architecture from one continuous power line to a power line in which a periodic array of discrete shunt-like sensors is contacted in parallel. Such discrete configuration will further enhance sensitivity, reduce the noise, and enable the shift from analog to digital operation scheme.

6 Conclusion

In this study, we present a novel multimodal fiber antenna designed for real-time pressure and proximity monitoring along the fiber. TDR analysis of the fiber antenna exhibits a sensitivity

of 0.274 kPa and a spatial resolution of 1.4 cm at a signal-to-noise ratio of one when operated in a fiber-mode superposition coupling scheme. The COMSOL Multiphysics simulations evaluating the symmetric and antisymmetric modes of the fiber antenna demonstrate that the symmetric mode effectively detects pinch stress, whereas the antisymmetric mode detects foreign objects in fiber proximity.

The electromagnetic coupling scheme used in this study to generate mixed-fiber modes will be adapted according to the outcomes obtained from the fiber mode simulations, aiming to form symmetric and antisymmetric fiber modes individually in future investigations and new device development. Moreover, it is noteworthy that the proximity sensing results of the multimodal fiber antenna reveal its capability for material identification due to the distinguishable difference between the signal peaks generated by metal weights and fingers in close fiber proximity.

The pressure-sensing outcomes obtained from pressure sending using the multimodal fiber antenna suggest its potential for real-time monitoring of hydrostatic measurements in liquids and blood pressure, which is particularly applicable in biomedical settings.

However, to succeed toward this end, porosity introduced into the fiber cladding is a necessary condition for increasing the fiber compressibility, and thus sensitivity to deformation under hydrostatic, omni-directional pressure conditions, unlike in this study, where pinch-stress application was clearly directional. In this study, we found that the current fiber is highly deformable, yet at the same time is also almost incompressible under hydrostatic and isotropic pressure. We have demonstrated in the measurements in Figs. 5(a) and 5(b) that the fiber's Poisson ratio is ∼0.5, which is the definition of a hardly compressible material.

A wide range of stress, temperature, proximity, and material identification detectors have been developed in the last few years. These include resistive,[6,37] mechanical-resonance,[38,39] capacitive,[28,40] and various optical[41–43] and plasmonic sensors.[44–46] All of them, to our best knowledge, are detectors with either optimized sensitivity for a single-point measurement or distributed detectors that are either limited by signal-propagation losses in the ability to measure gradiometrically over large distances, such as near-infrared-to-visible plasmonic gas detectors[44] or demonstrate limited spatial resolution (order of 1 m), such as optical fiber-based stress/deformation sensors.[29,41,47]

We demonstrate in this study that GHz/sub-THz range fibers of the kind that are presented in this paper uniquely combine the four important characteristics simultaneously: large propagation distances (meters to tens of meters with no major signal loss); high spatial resolution (centimetric, and, potentially, millimetric); high signal sensitivity (pressure sensitivity of 0.26 kPa demonstrated in this paper is equivalent to ±1 mmHg); and, finally, ability to choose functional modality (pressure/proximity sensing) by choosing the electromagnetic radiation mode to which the signal is coupled (antisymmetric/symmetric mode).

Code and Data Availability

The data that support the findings of this study are openly available in the figshare repository at Ref. 48.

Acknowledgments

This work was funded by Cook Medical Inc. We would like to acknowledge the Nanoscale Characterization Facility at Indiana University for their help in collecting the scanning electron microscopy images of the multimodal fiber antenna.

References

1. J. Zhang et al., "Advanced multi-material optoelectronic fibers: a review," *J. Lightwave Technol.* **39**, 3836–3845 (2021).
2. W. Yan et al., "Thermally drawn advanced functional fibers: new frontier of flexible electronics," *Mater. Today* **35**, 168–194 (2020).
3. W. Yan et al., "Advanced multimaterial electronic and optoelectronic fibers and textiles," *Adv. Mater.* **31**, 1802348 (2019).
4. A. F. Abouraddy et al., "Towards multimaterial multifunctional fibres that see, hear, sense and communicate," *Nat. Mater.* **6**(5), 336–347 (2007).
5. M. Chen et al., "Elastic and stretchable functional fibers: a review of materials, fabrication methods, and applications," *Adv. Fiber Mater.* **3**, 1–13 (2021).
6. A. Leber et al., "Soft and stretchable liquid metal transmission lines as distributed probes of multimodal deformations," *Nat. Electron.* **3**(6), 316–326 (2020).
7. W. Ryu et al., "Thermally drawn multi-material fibers based on polymer nanocomposite for continuous temperature sensing," *Adv. Fiber Mater.* **5**, 1712–1724 (2023).
8. Y. He et al., "Thermally drawn super-elastic multifunctional fiber sensor for human movement monitoring and joule heating," *Adv. Mater. Technol.* **8**, 2202079 (2023).
9. H. Banerjee et al., "Soft multimaterial magnetic fibers and textiles," *Adv. Mater.* **35**, 2212202 (2023).
10. A. Gumennik et al., "All-in-fiber chemical sensing," *Adv. Mater.* **24**, 6005–6009 (2012).
11. G. Loke et al., "Recent progress and perspectives of thermally drawn multimaterial fiber electronics," *Adv. Mater.* **32**, 1904911 (2020).
12. Y. Qu et al., "Superelastic multimaterial electronic and photonic fibers and devices via thermal drawing," *Adv. Mater.* **30**, 1707251 (2018).
13. C. Zhu et al., "Advanced fiber materials for wearable electronics," *Adv. Fiber Mater.* **5**, 12–35 (2023).
14. C. Lu et al., "Flexible and stretchable nanowire-coated fibers for optoelectronic probing of spinal cord circuits," *Sci. Adv.* **3**, e1600955 (2017).
15. C. Faccini de Lima et al., "Towards digital manufacturing of smart multimaterial fibers," *Nanosc. Res. Lett.* **14**, 209 (2019).
16. A. Gumennik et al., "Very large-scale integration for fibers (VLSI-Fi)," Patent US11692855B2 (2023).
17. S. Aoki, "Biorender," 2024, https://www.biorender.com/ (accessed 21 July 2024).
18. L. A. van der Elst et al., "Microstructured electroceutical fiber-device for inhibition of bacterial proliferation in wounds," *Adv. Mater. Interfaces* **10**, 2201854 (2023).
19. L. van der Elst et al., "3D printing in fiber-device technology," *Adv. Fiber Mater.* **3**(2), 59–75 (2021).
20. V. N. Koraganji et al., "Effects of 3D printed preform annealing on structural and optical properties of fibers," in *14th Pac. Rim Conf. Lasers and Electro-Opt. (CLEO PR 2020)*, p. C6H_6 (2020).
21. G. Tao, A. M. Stolyarov, and A. F. Abouraddy, "Multimaterial fibers," *Int. J. Appl. Glass Sci.* **3**, 349–368 (2012).
22. G. Goubau, "Surface waves and their application to transmission lines," *J. Appl. Phys.* **21**(11), 1119–1128 (1950).
23. S. K. Oruganti et al., "Experimental realization of Zenneck type wave-based non-radiative, non-coupled wireless power transmission," *Sci. Rep.* **10**(1), 1–12 (2020).
24. D. M. Pozar, *Microwave Engineering*, Wiley (2012).
25. S. Littmarck and F. Saeidi, "COMSOL Multiphysics 6.2," 2024, https://www.comsol.com/ (accessed 21 July 2024).
26. Y. A. Ilarionov et al., "The fundamental electromagnetic wave of a single-wire line in a weakly absorbing medium," *J. Commun. Technol. Electron.* **52**, 140–146 (2007).

27. L. A. van der Elst et al., "Rapid fabrication of sterile medical nasopharyngeal swabs by stereolithography for widespread testing in a pandemic," *Adv. Eng. Mater.* **22**, 2000759 (2020).
28. L. Yu et al., "Flexible multi-material fibers for distributed pressure and temperature sensing," *Adv. Funct. Mater.* **30**, 1908915 (2020).
29. J. P. Moore et al., "Shape sensing using multi-core fiber optic cable and parametric curve solutions," *Opt. Express* **20**(3), 2967–2973 (2012).
30. Y. Li et al., "Smart glove integrated with tunable MWNTs/PDMS fibers made of a one-step extrusion method for finger dexterity, gesture, and temperature recognition," *ACS Appl. Mater. Interfaces* **12**, 23764–23773 (2020).
31. T. Bao, J. Wang, and Y. Yao, "A fiber optic sensor for detecting and monitoring cracks in concrete structures," *Sci. China Technol. Sci.* **53**, 3045–3050 (2010).
32. C. Faccini de Lima et al., "Multimaterial fiber as a physical simulator of a capillary instability," *Nat. Commun.* **14**(1), 1–17 (2023).
33. A. Gumennik et al., "Silicon-in-silica spheres via axial thermal gradient in-fibre capillary instabilities," *Nat. Commun.* **4**, 2216 (2013).
34. A. Gumennik et al., "Confined in-fiber solidification and structural control of silicon and silicon−germanium microparticles," *PNAS* **114**, 7240–7245 (2017).
35. C. Faccini de Lima et al., "Creating fiber-embedded photonic circuitry by liquid-phase structuring of multi-material cores," *Proc. SPIE* **12433**, 1243307 (2023).
36. L. Wei et al., "Optoelectronic fibers via selective amplification of in-fiber capillary instabilities," *Adv. Mater.* **29**, 1603033 (2017).
37. L. Pan et al., "An ultra-sensitive resistive pressure sensor based on hollow-sphere microstructure induced elasticity in conducting polymer film," *Nat. Commun.* **5**(1), 1–8 (2014).
38. Y. Richter, E. S. Tammam, and S. E. Mandel, "Method of detecting portal and/or hepatic pressure and a portal hypertension monitoring system," Patent Application WO2013033506A1 (2013).
39. P. Song et al., "Recent progress of miniature MEMS pressure sensors," *Micromachines* **11**, 56 (2020).
40. J. Lee et al., "Conductive fiber-based ultrasensitive textile pressure sensor for wearable electronics," *Adv. Mater.* **27**, 2433–2439 (2015).
41. K. Sui et al., "In vivo brain temperature mapping using polymer optical fiber Bragg grating sensors," *Opt. Lett.* **48**(16), 4225–4228 (2023).
42. Z. Jin et al., "Silicon photonic integrated interrogator for fiber-optic distributed acoustic sensing," *Photonics Res.* **12**(3), 465–473 (2024).
43. P. Lu et al., "Distributed optical fiber sensing: review and perspective," *Appl. Phys. Rev.* **6**, 41302 (2019).
44. F. A. A. Nugroho et al., "Inverse designed plasmonic metasurface with parts per billion optical hydrogen detection," *Nat. Commun.* **13**(1), 1–10 (2022).
45. S. N. Khonina et al., "Plasmonic sensor based on metal-insulator-metal waveguide square ring cavity filled with functional material for the detection of CO_2 gas," *Opt. Express* **29**(11), 16584–16594 (2021).
46. R. S. El Shamy, D. Khalil, and M. A. Swillam, "Mid infrared optical gas sensor using plasmonic Mach-Zehnder interferometer," *Sci. Rep.* **10**(1), 1–9 (2020).
47. A. Gillooly, "Fiber sensing: medical fiber-optic sensors offer haptics, 3D shape sensing, and pressure sensing – Laser Focus World," 2016, https://www.laserfocusworld.com/fiber-optics/article/16546889/fiber-sensing-medical-fiber-optic-sensors-offer-haptics-3d-shape-sensing-and-pressure-sensing (accessed 21 July 2024).
48. M. Gokce et al., "Multimodal fiber antenna for proximity and stress sensing: source data," (dataset), https://figshare.com/articles/dataset/Multimodal_fiber_antenna_for_proximity_and_stress_sensing_source_data/26339773 (2024).

Biographies of the authors are not available.